Chinese Journal of
POLYMER SCIENCE

RESEARCH ARTICLE

https://doi.org/10.1007/s10118-026-3580-2
Chinese J. Polym. Sci. **2026**, *44*, 1186–1198

Synergistic Bioinspired Interface and Segregated Graphene Oxide Networks Enabling Enhanced Mechanical Strength and Chemical Resistance in Natural Rubber Latex Composites

Xiao-Da Pan[a,†], Yun-Kui Song[b,†], Chong-Zhi Sun[b], Chao-Yang Yuan[a], Zong-Min Zhu[a], Jia-Ran Wang[c], Xian-Ze Yin[a], Hong-Tao Liu[a*], Li Liu[b*], and Long Zheng[a*]

[a] *Hubei Key Laboratory for New Textile Materials and Applications, College of Materials Science and Engineering, Wuhan Textile University, Wuhan 430200, China*
[b] *State Key Laboratory of Organic-Inorganic Composites, Beijing University of Chemical Technology, Beijing 100029, China*
[c] *School of Materials Science and Engineering, Beijing University of Chemical Technology, Beijing 102202, China*

Abstract Natural rubber (NR) latex is a renewable colloidal dispersion used in medical gloves, coatings, and flexible products. It is known for its excellent elasticity and film-forming ability but is limited by insufficient mechanical robustness and chemical resistance. Incorporating nanofillers, such as graphene oxide (GO), is an effective approach to enhance its performance; however, achieving strong interfacial compatibility between hydrophilic GO and the nonpolar rubber matrix remains challenging. To overcome this issue, a multifunctional interfacial design inspired by mussel adhesion chemistry was developed to construct a hierarchical and cohesive GO network within the NR latex matrix. A tannic acid-based modifier (TM) bearing catechol and thiol groups was synthesized and anchored onto latex particles *via* hydrogen bonding with surface proteins and phospholipids, enabling subsequent π–π interactions and hydrogen bonding with GO nanosheets. This guided the selective self-assembly of GO into a continuous segregated network along the latex particle boundaries. Hierarchical interface reinforcement was achieved through Eu^{3+} ligand coordination. The incorporation of GO and enhancement of interfacial interactions promoted strain-induced crystallization, resulting in increased crystallinity and improved load transfer. The resulting composite film containing 0.5 part per hundred rubber GO and the bioinspired interface exhibited a tensile strength that was 107.8% higher than that of the pure NR latex film, while maintaining an elongation at break of 915%. Tear strength increased by 118.5%, toughness reached 61.7 MJ/m^3, nitrogen permeability decreased by 20.1%, and antibacterial efficiency against both *Escherichia coli* and *Staphylococcus aureus* reached 99.9%. The films also exhibited enhanced resistance to organic solvents, acids, and alkalis. This study provides a green and scalable strategy for fabricating high-performance NR latex-based products suitable for medical, protective, and engineering applications.

Keywords Natural rubber latex; Mussel-inspired interface; Graphene oxide; Segregated filler network; Mechanical property

Citation: Pan, X. D.; Song, Y. K.; Sun, C. Z.; Yuan, C. Y.; Zhu, Z. M.; Wang, J. R.; Yin, X. Z.; Liu, H. T.; Liu, L.; Zheng, L. Synergistic bioinspired interface and segregated graphene oxide networks enabling enhanced mechanical strength and chemical resistance in natural rubber latex composites. *Chinese J. Polym. Sci.* **2026**, *44*, 1186–1198.

INTRODUCTION

Natural rubber (NR) latex, a sustainable colloidal dispersion derived from *Hevea brasiliensis*, is widely employed in medical membranes, protective gloves, coatings, and dipped goods owing to its superior film-forming capability and intrinsic elasticity.[1,2] These functional properties originate from their distinctive microstructure: biosynthesized *cis*-1,4-polyisoprene chains stabilized by 5 wt%–10 wt% non-rubber components, including proteins, phospholipids, and inorganic salts. These non-rubber constituents interact with the polymer chain ends, enabling strain-induced crystallization and mechanical resilience.[3,4] Despite these advantages, NR films exhibit inherent limitations such as inadequate mechanical robustness, low chemical resistance, and poor barrier and antibacterial properties, restricting their application in demanding fields such as protective gloves and flexible electronics.[5] Consequently, the development of high-performance NR composite films with multifunctional enhancements is a key research objective.

Nanofiller incorporation is a proven strategy for improving the performance of rubber.[6] Hydrophilic fillers, such as graphene oxide (GO),[7] MXene,[8] and biomass fillers[9–11] are compatible with aqueous NR latex systems. Nevertheless, their polar nature compromises the interfacial compatibility with nonpolar polyisoprene chains, leading to filler aggregation during film formation.[12–14] Moreover, low-aspect-ratio fillers often require high loadings to achieve effective rein-

* Corresponding authors, E-mail: lht@wtu.edu.cn (H.T.L.)
E-mail: liul@mail.buct.edu.cn (L.L.)
E-mail: lzheng@wtu.edu.cn (L.Z.)
† These authors contributed equally to this work.
Received November 13, 2025; Accepted January 17, 2026; Published online March 10, 2026

forcement, which can compromise latex coalescence and film integrity.[15] While GO offers a two-dimensional morphology and a high modulus advantageous for reinforcement, its loading must typically remain below 1 part per hundred rubber (phr) to avoid embrittlement.[16,17] Thus, strategies that maximize the reinforcement efficiency at minimal filler content are essential.

The construction of a three-dimensional (3D) segregated filler network within rubber composites has emerged as a promising approach. Unlike randomly dispersed fillers, segregated networks form when nanofillers preferentially localize at the interfaces between adjacent latex particles, creating a continuous, interconnected framework. Such architectures have been shown to provide superior reinforcement compared with uniform dispersions.[18–22] For example, George *et al*.[20] employed poly(ethylene oxide) as a nonionic surfactant to disperse multi-walled carbon nanotubes (MWCNTs) in water and fabricate MWCNT/NR composites with a segregated network through latex blending and film casting, achieving notable improvements in mechanical, thermal, electrical, and barrier properties owing to the well-defined segregated filler architecture. Notably, the colloidal nature of NR latex intrinsically facilitates network templating; however, hydrophilic filler-rubber incompatibility often disrupts network formation during drying, underscoring the need for precise interfacial engineering.

In this study, we exploited a mussel-inspired interfacial strategy to overcome filler-matrix incompatibility and enable efficient segregated network formation. Drawing inspiration from the adhesive proteins found in mussels, which employ catechol groups to form strong bonds through hydrogen bonding, coordination, and π-π interaction[23,24], a bioinspired modifier (TM) was synthesized by conjugating tannic acid (TA) with γ-mercaptopropyltrimethoxysilane (MPS). The catechol moieties facilitate adhesion to NR latex surface proteins and phospholipids, while the thiol groups subsequently participate in covalent thiol-ene crosslinking during vulcanization. Following TM adsorption, GO nanosheets were anchored onto the TM layer *via* π-π interactions and hydrogen bonding, directing their self-assembly into a continuous 3D segregated network templated by latex particles. To strengthen the hierarchical interface further, trivalent Eu ions (Eu^{3+}) were introduced. Owing to their unique 4f electron configuration, Eu^{3+} ions can form strong coordination interactions with catechol and hydroxyl groups on the TM and GO surfaces, thereby reinforcing interfacial cohesion and stabilizing the segregated GO network. This hierarchical interfacial design enables systematic regulation of the network morphology and interfacial interactions, leading to enhanced mechanical strength, gas barrier performance, chemical resistance, and antibacterial activity of the NR composites, and provides a viable strategy for multifunctional rubber systems.

EXPERIMENTAL

Materials

NR latex with a solid content of 60 wt% was purchased from Maoming Zhengmao Petrochemical Co., Ltd. (Guangdong, China). The NR latex was pre-vulcanized and had a solids content of 55%. Graphene oxide (GO) was supplied by Sixth Element Materials Technology Co., Ltd. (Changzhou, China). TA, MPS, europium nitrate hexahydrate ($Eu(NO_3)_3{\cdot}6H_2O$), and nonylphenol ethoxylate-10 (OP-10) were purchased from Shanghai Aladdin Bio-Chem Technology Co., Ltd. (Shanghai, China). Chloroform, *n*-hexane, mineral oil, hydrochloric acid, and sodium hydroxide were provided by the Wuhan Xinshenshi Chemical Technology Co., Ltd. All chemicals were used as received.

Preparation of TM Aqueous Solution and TMNR Latex

The aqueous TM solution was prepared as follows. Initially, 1 g of TA was completely dissolved in 48 g of deionized water under continuous stirring at ambient temperature. Then, MPS (1 g) was slowly added dropwise to the TA solution under vigorous stirring. The mixture was thermally reacted at 60 °C for 6 h in a temperature-controlled reactor, obtain the TM aqueous solution. After cooling to room temperature, 50 g of the resulting TM aqueous solution was blended into the pre-vulcanized NR under constant stirring for 30 min while maintaining a rubber-to-TM mass ratio of 100:2. The TM-modified NR (denoted as TMNR) was then obtained.

Preparation of GO/NR, GO/TMNR and GO/TMNR-Eu^{3+} Composite Films

A homogeneous GO dispersion (0.4 wt%) was prepared *via* ultrasonication for 30 min. To fabricate the GO/TMNR composite films, TMNR (containing 10 g of NR solids) was blended with a predetermined amount of GO dispersion under mechanical stirring at room temperature for 30 min. The resulting latex suspension was cast into a glass culture dish and dried under ambient conditions until complete evaporation of water. The dried films were thermally cured at 120 °C for 20 min in a vacuum oven to obtain GO/TMNR films with GO loadings of 0.1, 0.3 and 0.5 phr, respectively.

For the preparation of the GO/TMNR-Eu^{3+} composite films, 0.024 g of $Eu(NO_3)_3{\cdot}6H_2O$ was added to the GO/TMNR suspension and stirred for 30 min. To avoid latex destabilization induced by the addition of Eu^{3+}, 1 phr of the nonionic surfactant OP-10 was premixed into the latex system before Eu^{3+} addition. Film casting and curing were performed as previously described.

As a control group, GO/NR composite films were obtained by directly blending a GO dispersion with pre-vulcanized NR latex, followed by the same film-casting procedure, without TM or Eu^{3+} incorporation. All the composite films were designated as GO/NR-*x*, GO/TMNR-*x*, and GO/TMNR-Eu^{3+}-*x*, where x represents the GO loading (phr) in the final rubber composites.

Characterization

Ultraviolet-visible (UV-Vis) spectroscopy was performed using a Jasco J-670 spectrophotometer (JASCO Corporation, Japan). X-ray diffraction (XRD) measurements were performed using a D/Max-2500 diffractometer (Rigaku Corporation, Japan). Attenuated total reflectance Fourier-transform infrared (ATR-FTIR) spectroscopy was performed using a Spectrum 100 spectrometer (PerkinElmer, USA). X-ray photoelectron spectroscopy (XPS) was conducted using an ESCALAB 250 XPS system (Thermo Fisher Scientific, USA) with an Al Kα X-ray source (1486.6 eV). Atomic force microscopy (AFM) was performed using the peak force quantitative nanomechanical mapping mode on a MultiMode 8 AFM system (Bruker Corporation, USA). The samples

https://doi.org/10.1007/s10118-026-3580-2

were cryo-fractured using a Leica EM FC7 ultramicrotome to obtain flat surfaces. Transmission electron microscopy (TEM) was performed using a Tecnai G2 20 S-TWIN microscope (FEI Company, USA) at an accelerating voltage of 300 kV. Dynamic mechanical analysis (DMA) was performed using a VA3000 analyzer (01dB-Metravib, France) in tensile mode at a frequency of 10 Hz over a temperature range from −80 °C to 80 °C, with a heating rate of 3 °C/min. The tensile properties of the dumbbell-shaped specimens were evaluated using an Instron 4465 universal testing machine (Instron Corporation, USA), in accordance with ISO 37:2011. Gas permeability was tested using a VAC-V2 gas permeability tester (Labthink Instruments Co., Ltd., China) at 40 °C in accordance with ISO 2782. Antibacterial performance against *Escherichia coli* (*E. coli*) and *Staphylococcus aureus* (*S. aureus*) was assessed following the JIS Z 2801:2012 standard.

The strain-induced crystallization (SIC) behavior of rubber films was investigated using two-dimensional wide-angle X-ray diffraction (2D-WAXD). The measurements were performed using a Rigaku HomeLab X-ray diffractometer equipped with a HyPix-6000 photon-counting detector. Cu Kα radiation with a wavelength of 1.5405 Å was used as the X-ray source. The detector pixel size was 100 μm × 100 μm. Data processing and analysis were performed using Fit2D software. The crystallinity index (CI) was determined after peak separation fitting of the diffraction profiles and was calculated according to the following equation: [25]

$$\mathrm{CI} = \frac{\sum A_c}{\sum A_a + \sum A_c} \tag{1}$$

where $\sum A_c$ represents the sum of the peak areas corresponding to the 200, 201, and 120 crystal planes and $\sum A_a$ represents the peak area of the amorphous halo.

The crosslinking density was determined by equilibrium swelling in toluene. Pre-weighed film samples were immersed in toluene for 72 h at room temperature. After swelling, the samples were quickly wiped with filter paper to remove surface solvent, weighed immediately, and then dried in a vacuum oven at 60 °C until reaching a constant weight. The crosslink density (V_e) was calculated using the Flory-Rehner equation[26]

$$V_e = -\frac{\ln(1 - V_r) + V_r + \chi V_r^2}{V_1\left(V_r^{\frac{1}{3}} - \frac{V_r}{2}\right)} \tag{2}$$

where V_1 is the molar volume of toluene (106.2 cm^3/mol), χ is the Flory-Huggins interaction parameter (0.393 for NR and toluene[27]), and V_r is the volume fraction of rubber in the swollen gel, calculated by:

$$V_r = \frac{m_2/\rho_r}{m_2/\rho_r + (m_1 - m_0)/\rho_s} \tag{3}$$

where ρ_r is the density of NR (0.913 g/cm^3), ρ_s is the density of toluene (0.865 g/cm^3), m_0 is the initial dry weight, m_1 is the swollen weight, and m_2 is the final dry weight after swelling.

Solvent resistance was evaluated using square film samples (25 mm × 25 mm × 0.5 mm) immersed in solvents, including chloroform, *n*-hexane, and mineral oil. The degree of swelling was determined as the percentage increase in weight.

$$\text{Swelling degree} = \frac{W_i - W_0}{W_0} \times 100\% \tag{4}$$

where W_0 is the initial weight, and W_i is the weight after swelling for a specified duration.

Acid and alkali resistance was assessed by immersing dumbbell-shaped specimens in 0.1 mol/L HCl and 1 mol/L NaOH solutions for 1, 4, and 7 days at room temperature. After immersion, the samples were dried thoroughly and subjected to tensile testing. The retention of mechanical properties was then calculated to assess the material stability under acidic and alkaline conditions.

RESULTS AND DISCUSSION

Construction and Microstructure Characterization of NR Composite Films

As shown in Fig. 1(a), the GO/NR, GO/TMNR, and GO/TMNR-Eu^{3+} composite films were fabricated *via* distinct interfacial design strategies, with the corresponding interfacial interactions illustrated in Fig. 1(b). In the GO/NR system, GO nanosheets were directly blended with pre-vulcanized NR without interfacial modifiers, resulting in weak filler-matrix adhesion and a randomly distributed filler network. In contrast, the GO/TMNR and GO/TMNR-Eu^{3+} systems employ TM or TM combined with Eu^{3+} to establish multiple interfacial interactions, including hydrogen bonding, π-π interactions, and coordination bonding. TM, enriched in catechol groups, mimics the adhesive proteins found in mussels and enables strong attachment to latex particle surfaces *via* hydrogen bonding with surface proteins and phospholipids. During vulcanization, the thiol groups in TM participate in covalent thiol-ene reactions with the C=C bonds of polyisoprene, further consolidating the interface. This mussel-inspired interfacial layer acts as a molecular bridge, directing the selective self-assembly of GO nanosheets along the latex particle boundaries and promoting the formation of well-defined segregated networks. Furthermore, the incorporation of Eu^{3+} ions exploits their strong coordination capability with electron-donating groups, such as catechols and hydroxyls, further reinforcing the interfacial architecture, enhancing network stability, and improving the compatibility between GO and the latex matrix.

The synthesis was achieved *via* dehydration condensation between TA and MPS, as illustrated in Fig. 2(a). At 60 °C, the acidic environment provided by TA promoted the hydrolysis of MPS, generating silanol groups, which subsequently underwent dehydration condensation with the phenolic hydroxyl groups of TA to form TM. During the reaction, the color of the solution gradually changed from pale yellow to milky white, as shown in the inset photographs of Fig. 2(a). To further verify the reaction between TA and MPS, the FTIR spectra of TA, MPS, TM, and TA + MPS physical mixture, were compared (Fig. 2b). The TA + MPS physical mixture exhibited a simple superposition of the characteristic absorption bands of the two raw materials, with the Si—C band remaining at 782 cm^{-1}, indicating that only limited interaction occurred during physical mixing. In contrast, the Si—C band in TM shifted to 799 cm^{-1}, reflecting a change in the chemical environment of the Si—C groups associated with the reaction between TA and MPS. Combined with the macroscopic changes observed during synthesis, these spectral features support

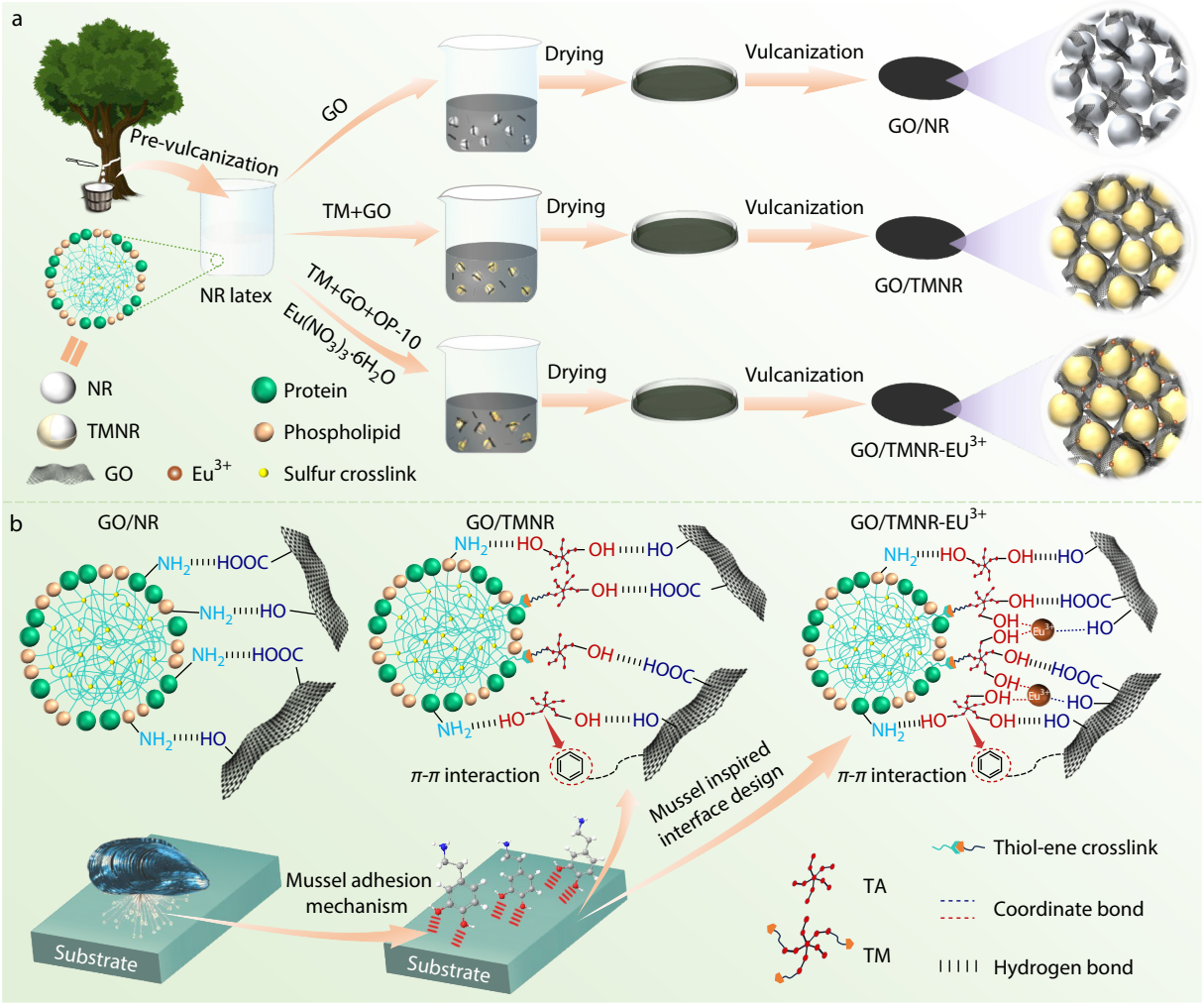

Fig. 1 (a) Schematic illustration of the fabrication processes for GO/NR, GO/TMNR, and GO/TMNR-Eu^{3+} composite films; (b) Schematic depiction of the interfacial interactions in GO/NR, GO/TMNR, and GO/TMNR-Eu^{3+} composite films.

the successful formation of TM and confirm the incorporation of MPS into the TA-based structure, while preserving key functional groups, such as phenolic hydroxyls (3284 cm^{-1}) from TA [28] and —SH (2553 cm^{-1}) from MPS.[29]

UV-Vis spectra (Fig. 2c) revealed TA absorption peaks at 213 nm (π–π * transitions from aromatic C=C bonds) and 276 nm (n-π* transitions associated with C—O bonds).[30] TM displayed a similar but more intense absorption, suggesting the preservation of TA-derived chromophores. GO exhibited a characteristic peak at 235 nm (aromatic C=C) and a shoulder at 301 nm (n–π* transitions).[31] Upon TM modification, TM-GO showed a blue shift to 216 nm (π-π*) and a red shift to 271 nm (n–π*), confirming the presence of non-covalent π–π and hydrogen bonding interactions between TM and GO.

The ATR-FTIR spectra of the composite films (Fig. 2d) exhibit characteristic peaks at 2960, 2911, and 2848 cm^{-1}, corresponding to the asymmetric stretching of —CH_3, asymmetric stretching of —CH_2, and symmetric stretching of —CH_2 in *cis*-1,4-polyisoprene, respectively.[32] Compared with NR, TMNR, and GO/TMNR–0.5, the O—H stretching vibration at 3287 cm^{-1} and a phenolic —OH stretching peak at 1206 cm^{-1} confirmed the successful anchoring of TM onto latex surfaces.[16] Upon Eu^{3+} incorporation, a slight decrease in the intensity and a red shift of the phenolic —OH band from 1206 cm^{-1} to 1192 cm^{-1}. Although these spectral changes are relatively minor, they qualitatively suggest possible coordination between Eu^{3+} ions and hydroxyl groups on the TM and GO.[33] The XRD patterns of all the films (Fig. 2e) displayed a broad diffraction peak around 19°, characteristic of the amorphous nature of the polyisoprene chains. The (002) reflection of GO (about 11°) was not observed, which can be attributed to the low GO loading and the effective dispersion of the GO nanosheets within the matrix.

The high-resolution C 1s XPS spectra of NR and TMNR (Figs. 2f and 2g) were deconvoluted into five components: C=C (284.2 eV), C—C (284.8 eV), C—S (285.5 eV), C—O (286.5 eV), and C=O (288.4 eV).[34] TM incorporation led to an increase in the relative proportion of C—S from 12.5% to 15.1%, accompanied by a decrease in the relative proportion of C=C from 33.3% to 23.9% (Table 1), suggesting partial consumption of unsaturated double bonds *via* thiol-ene reactions during vulcanization. Furthermore, equilibrium swelling analysis (Fig. 2h) revealed a substantial increase in crosslink density after TM and Eu^{3+} incorporation, which was attributed to the syn-

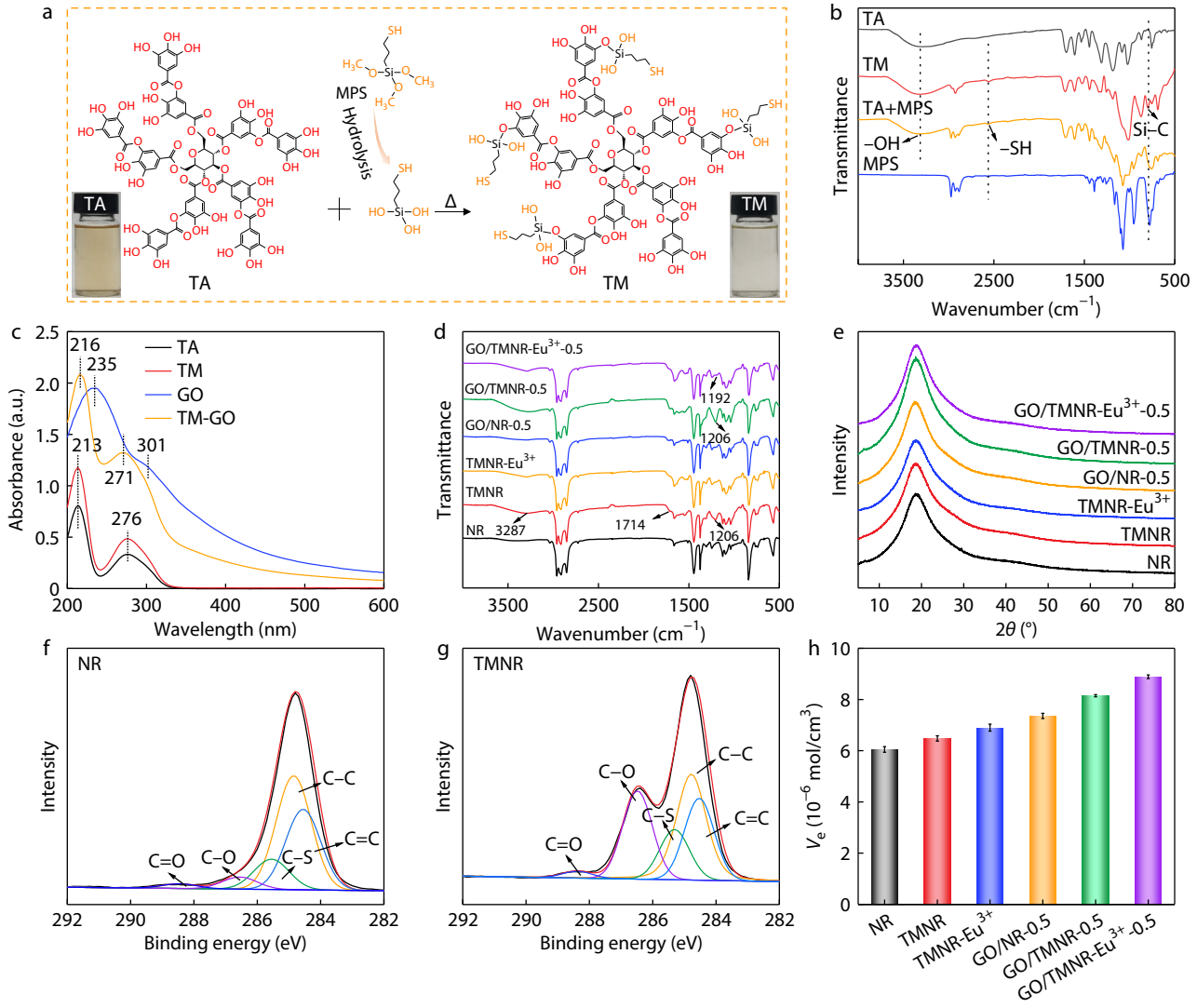

Fig. 2 (a) Schematic illustration of TM synthesis *via* the reaction between TA and MPS; insets are the picture of TA and TM solutions; (b) FTIR spectra of TA, MPS, TA+MPS physical mixture, and TM; (c) UV-Vis absorption spectra of TA, TM, GO, and TM-GO solutions; (d) ATR-FTIR spectra and (e) XRD patterns of NR composite films; C 1s XPS spectra of (f) NR and (g) TMNR with peak deconvolution; (h) Crosslink density of NR composite films.

Table 1 Quantitative analysis of C 1s XPS peak of NR and TMNR films.

Bond type	Binding energy (eV)	NR	TMNR
		Peak area (%)	Peak area (%)
C=C	284.2	33.3	23.9
C–C	284.8	47.2	32.7
C–S	285.5	12.5	15.1
C–O	286.5	5.0	25.6
C=O	288.4	1.9	2.8

ergistic contribution of covalent thiol-ene crosslinking and additional non-covalent interactions.

AFM images (Figs. 3a–3c) revealed that the root mean square (RMS) surface roughness increases from 5.9 nm for NR to 9.2 nm for TMNR and further to 12.7 nm for TMNR-Eu^{3+}. This progressive roughening is attributed to the adsorption of TM and subsequent Eu^{3+} coordination at the latex surfaces, which enhances the interfacial heterogeneity and provides abundant anchoring sites for the GO nanosheets. Although GO carries abundant oxygen-containing functional groups capable of forming hydrogen bonds with proteins and phospholipids on NR particles, such hydrogen-bonding interactions alone are insufficient for suppressing GO stacking during film formation and drying. As water evaporates, the electrostatic repulsion between the GO sheets diminishes, enabling intrinsic π-π stacking to dominate and induce aggregation.[13] This aggregation disrupts the templating effect of latex particles, preventing the formation of a well-defined segregated filler network. As shown in Fig. 3(d), the TEM image of the GO/NR-0.5 composite displays GO sheets (dark lines) randomly dispersed and agglomerated rather than assembling around latex particles. In contrast, TM adsorption on latex surfaces formed a distinct light-grey interfacial layer surrounding the particles (Fig. 3e), confirming successful TM anchoring. Acting as a mussel-inspired molecular bridge, this TM layer promotes strong interfacial adhesion and drives the self-as-

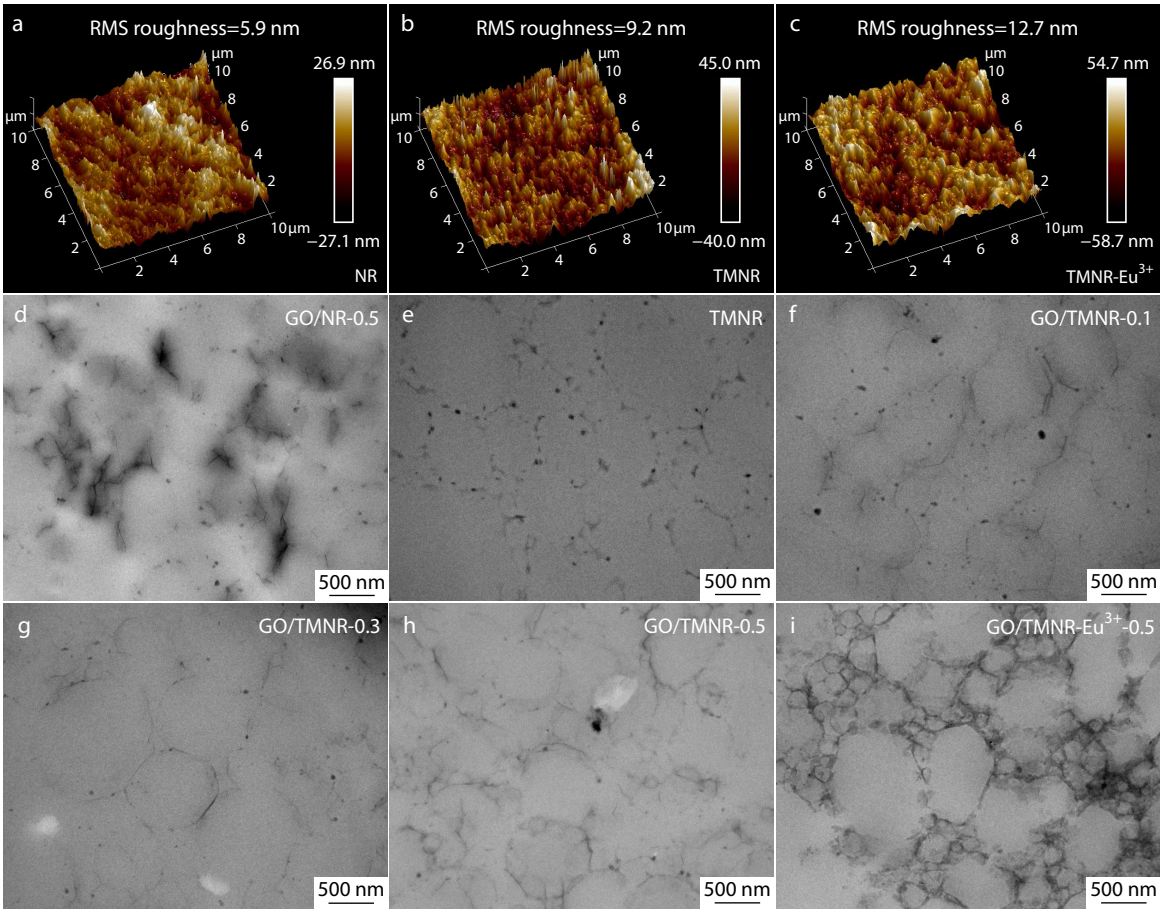

Fig. 3 AFM images of (a) NR, (b) TMNR, and (c) TMNR-Eu^{3+} films; TEM images of (d) GO/NR-0.5, (e) TMNR, (f) GO/TMNR-0.1, (g) GO/TMNR-0.3, (h) GO/TMNR-0.5, and (i) GO/TMNR-Eu^{3+}-0.5 composite films.

sembly of GO into segregated architecture. Even at a low GO content (0.1 phr, the GO nanosheets were uniformly distributed around the latex particles (Fig. 3f), demonstrating efficient network formation guided by the TM interface. With increasing GO content to 0.3 and 0.5 phr, the segregated network becomes progressively more continuous and densely interconnected (Figs. 3g and 3h), highlighting the effectiveness of TM-mediated assembly. The incorporation of Eu^{3+} further amplifies this effect by introducing metal-ligand coordination at the interface. As shown in Fig. 3(i), GO/TMNR-Eu^{3+}-0.5 exhibited pronounced interfacial microdomains and thickened interfacial regions, indicating a robust interfacial reinforcement. The combined mussel-inspired adhesion and Eu^{3+} coordination synergistically stabilized the segregated GO network, enhanced its structural integrity, and improved its compatibility with the latex matrix, thereby establishing a hierarchical interface that is essential for maximizing the multifunctional performance of the composite.

Mechanical Properties of the NR Composite Films

Tensile tests were performed to elucidate the effects of interfacial engineering and segregated filler networks on the mechanical properties of the NR composite films (Figs. 4a–4c). Across the GO/NR, GO/TMNR, and GO/TMNR-Eu^{3+} systems, the stress-strain curves exhibited similar profiles, with the tensile strength increasing and elongation at break decreasing as the GO content increased. However, the GO/TMNR and GO/TMNR-Eu^{3+} composites consistently achieved greater strength enhancement than GO/NR, underscoring the role of the strengthened interfacial interactions. TM modification increased the tensile strength of NR from 10.2 MPa to 12.5 MPa, and subsequent Eu^{3+} coordination further elevated it to 16.3 MPa, reflecting the combined contributions of thiol-ene crosslinking, hydrogen bonding, and metal-ligand coordination. Upon incorporating 0.5 phr GO, the tensile strength reached 13.5 MPa for GO/NR-0.5, 18.4 MPa for GO/TMNR-0.5, and 21.2 MPa for GO/TMNR-Eu^{3+}-0.5, representing increases of 32.4%, 80.4%, and 107.8% relative to NR. Similarly, the 300% modulus increased by 89.4%, 147.0%, and 251.5%, respectively, which was attributed to the synergistic effects of robust interfacial bonding and efficient stress transfer through the segregated GO network. Importantly, despite the modulus enhancement, the composites retained remarkable ductility with GO/TMNR-Eu^{3+}-0.5, exhibiting an elongation at break of 915%. The toughness and tear strength trends (Figs. 4d and 4e) further validated the effectiveness of the hierarchical interface design. GO/TMNR-Eu^{3+}-0.5 exhibited a toughness of 61.7 MJ/m^3, which was markedly higher than that of the pristine NR. This improvement is ascribed to the incorporation of sacrificial hydrogen and coordination bonds that rupture prior to covalent bonds, dissipating strain energy and enhancing toughness. In addition, the segregated GO network acted as a

https://doi.org/10.1007/s10118-026-3580-2

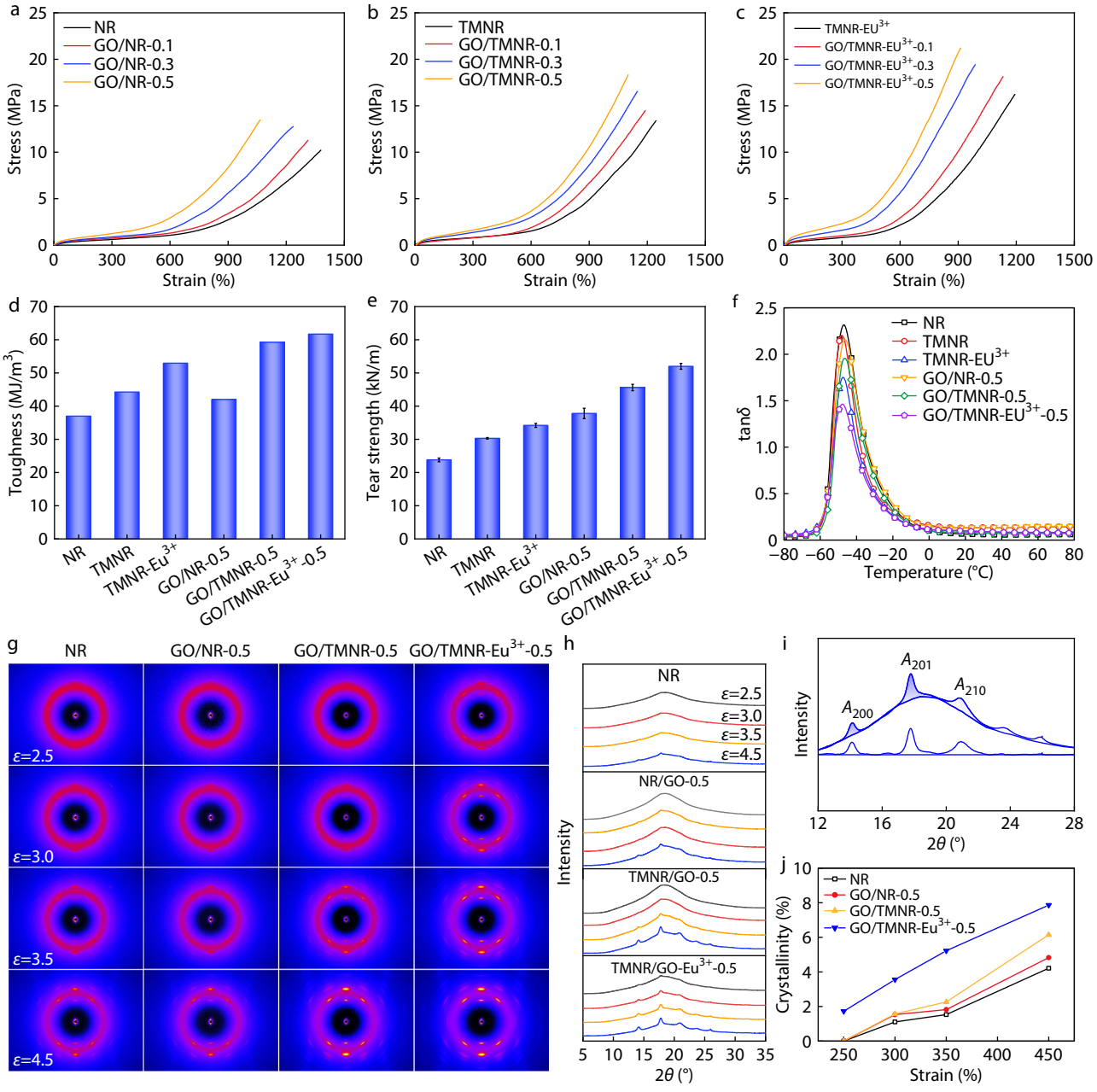

Fig. 4 (a) Stress-strain curves of (a) GO/NR, (b) GO/TMNR, and (c) GO/TMNR-Eu^{3+} composite films with different GO contents; Comparison of (d) toughness and (e) tear strength of NR, TMNR, TMNR-Eu^{3+}, GO/NR-0.5, GO/TMNR-0.5, and GO/TMNR-Eu^{3+}-0.5 composite films; (f) DMA tanδ versus temperature curves of NR, TMNR, TMNR-Eu^{3+}, GO/NR-0.5, GO/TMNR-0.5, and GO/TMNR-Eu^{3+}-0.5 composite films; (g) 2D-WAXD patterns of NR, GO/NR-0.5, GO/TMNR-0.5, and GO/TMNR-Eu^{3+}-0.5 at different strains. The label "ε=2.5" means that the strain equals 250%; (h) 1D-WAXD patterns of NR, GO/NR-0.5, GO/TMNR-0.5, and GO/TMNR-Eu^{3+}-0.5; (i) Demonstration for a typical deconvoluted 1D WAXD profile of NR, GO/NR-0.5, GO/TMNR-0.5, and GO/TMNR-Eu^{3+}-0.5; (j) Crystallinity index of NR, GO/NR-0.5, GO/TMNR-0.5, and GO/TMNR-Eu^{3+}-0.5 as a function of strain.

barrier to crack propagation, yielding tear strength increases of 98.3% and 118.9% for GO/TMNR-0.5 and GO/TMNR-Eu^{3+}-0.5, respectively, both surpassing the 69.6% improvement observed for GO/NR-0.5.

The mechanical performance of NR composites is governed by both filler-rubber interfacial interactions and SIC behavior. The interfacial interactions in the NR composites were evaluated by DMA. As shown in Fig. 4(f), the tanδ peak progressively decreased with the introduction of TM modification, GO incorporation, and Eu^{3+} coordination, indicating increasingly restricted chain mobility owing to the formation of a GO segregated network and strengthened interfacial constraints. The influence of such interfacial interactions on the SIC behavior of the NR composites was further investigated by *in situ* WAXD measurements. During tensile deformation, the SIC of the sample was continuously monitored, and the representative 2D-WAXD patterns are shown in Fig. 4(g). For all samples, highly oriented crystalline diffraction arcs gradu-

ally appeared after critical deformation and intensified with increasing strain, confirming the occurrence of typical SIC behavior during stretching. For the pristine NR, discernible crystalline arcs were observed only when the strain exceeded 300%. Upon the addition of 0.5 phr GO, the SIC behavior of GO/NR-0.5 remained largely similar to that of the pristine NR. In contrast, after interfacial enhancement *via* TM incorporation and the promoted formation of a GO-segregated network, GO/TMNR-0.5, exhibited more pronounced crystalline arcs at strains above 300%. Notably, for GO/TMNR–Eu^{3+}-0.5, distinct crystalline arcs were detectable at a strain of 250%, demonstrating a significantly advanced onset of SIC.

To evaluate the effect of interfacial regulation on SIC quantitatively, the collected 2D-WAXD were integrated and converted into 1D-WAXD diffraction profiles (Fig. 4h). The resulting profiles were further deconvoluted into three crystalline reflections corresponding to the (120), (201), and (200) planes together with an amorphous NR halo, as illustrated in Fig. 4(i). Based on the relative areas of the crystalline and amorphous components, CI was calculated, and the CI evolution with strain is summarized in Fig. 4(j). At the same strain level, GO/TMNR-0.5 consistently exhibited higher CI values than pristine NR and GO/NR-0.5, indicating that enhanced interfacial interactions effectively promoted chain alignment and crystallization. Upon Eu^{3+} coordination, the CI value reached approximately 1.7% at a strain of 250%. This behavior suggests that coordination bond formation leads to stronger interfacial interactions, which synergistically facilitate the chain orientation. At a high strain of 450%, this promotion effect became even more pronounced, confirming that the strong interfacial interactions markedly enhanced the SIC of the NR composites.

Gas Barrier and Antibacterial Properties of the NR Composite Films

The gas barrier properties of the NR composite films are shown in Fig. 5(a). The nitrogen permeability coefficient of the pure NR film was measured at 5.96×10^{-17} $m^2/(s\cdot Pa)$. The incorporation of TM and Eu^{3+} resulted in a slight reduction in permeability, which can be attributed to the increased crosslinking density and stronger interparticle interactions, effectively decreasing the free volume within the rubber matrix. Interestingly, the permeability coefficient of TMNR-Eu^{3+} was nearly identical to that of GO/NR-0.5, suggesting that the enhanced interfacial cohesion in TMNR-Eu^{3+} yielded a barrier performance comparable to that achieved by the randomly dispersed GO network in GO/NR-0.5. A substantial improvement was observed when GO was introduced into the TMNR and TMNR-Eu^{3+} systems to construct segregated filler networks. The nitrogen permeability coefficients of GO/TMNR-0.5 and GO/TMNR-Eu^{3+}-0.5 decreased by 14.6% and 20.1%, respectively, relative to those of the pristine NR film. These enhancements stem from two cooperative mechanisms:

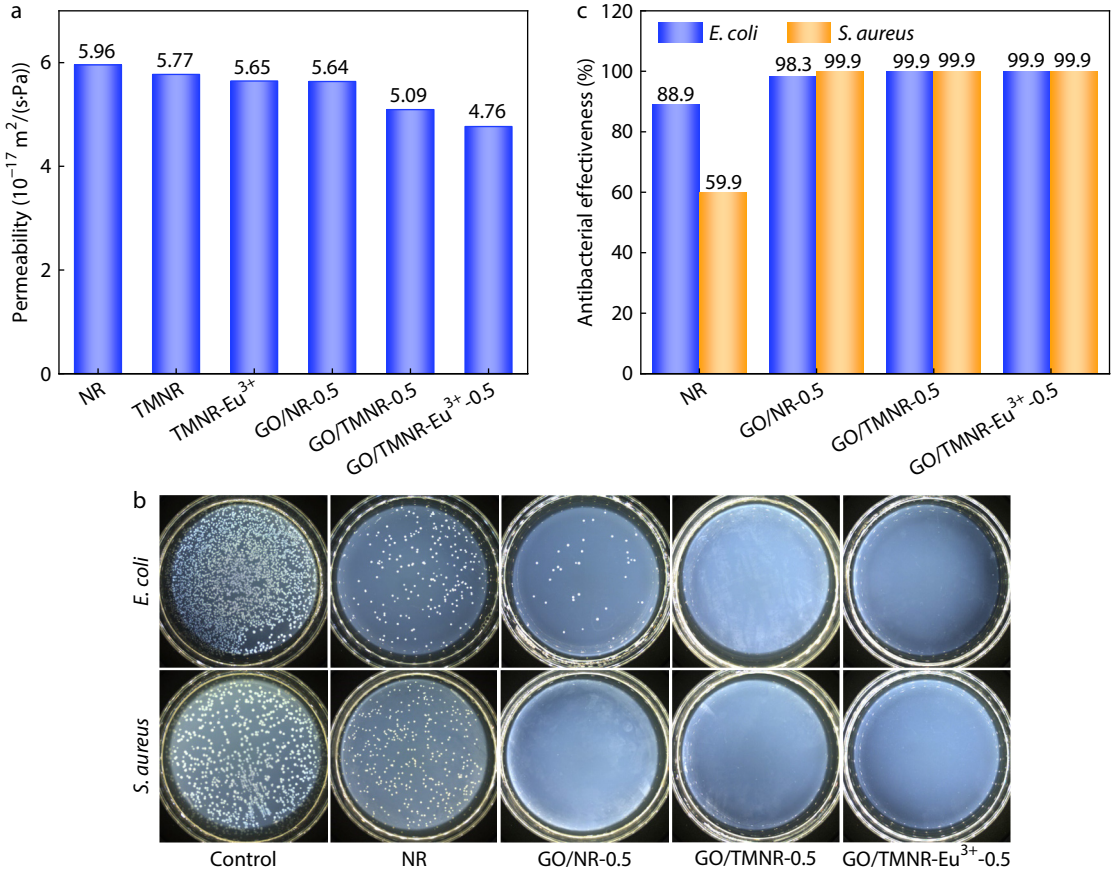

Fig. 5 (a) Nitrogen permeability of NR, TMNR, TMNR-Eu^{3+}, GO/NR-0.5, GO/TMNR-0.5, and GO/TMNR-Eu^{3+}-0.5 films; (b) Representative digital images of *E. coli* and *S. aureus* colonies on LB agar plates after exposure to various film samples; (c) Antibacterial effectiveness of the NR, GO/NR-0.5, GO/TMNR-0.5, and GO/TMNR-Eu^{3+}-0.5 against *E. coli* and *S. aureus*.

https://doi.org/10.1007/s10118-026-3580-2

(1) reduced molecular mobility due to strengthened interfacial interactions, which minimize inherent free volumes, and (2) increased diffusion tortuosity arising from the well-organized segregated GO network, which prolongs the effective gas permeation pathway.

Beyond the barrier properties, antibacterial performance is a crucial consideration for NR-based films, particularly in applications involving direct or indirect contact with the skin. Antibacterial activity was evaluated against representative Gram-negative *E. coli* and Gram-positive *S. aureus* (Figs. 5b and 5c). In the control group, extensive bacterial colonies were observed, whereas the pristine NR displayed only moderate antibacterial activity, achieving efficiencies of 88.9% and 59.9% against *E. coli* and *S. aureus*, respectively. The incorporation of GO into NR (GO/NR-0.5) enhanced its antibacterial activity to 98.3% and 99.9%, respectively. Remarkably, both GO/TMNR-0.5 and GO/TMNR-Eu^{3+}-0.5 exhibited complete inhibition (>99.9%) of both bacterial strains, with no visible colonies on the LB agar plates. This outstanding antibacterial performance arises from the synergistic contribution of the multiple functional components. TM modification retains phenolic hydroxyl groups from TA, which disrupts the peptidoglycan layer of the bacterial cell walls, leading to structural collapse.[35] Eu^{3+} ions interact electrostatically with negatively charged bacterial membranes, inducing the destabilization and leakage of intracellular contents. GO nanosheets provide a high surface area and sharp edges capable of physically piercing and fragmenting bacterial membranes.[36] The combination of these chemical and physical antibacterial mechanisms confers broad-spectrum and highly efficient antimicrobial protection. Consequently, the GO/TMNR-Eu^{3+}-0.5 films offer a rare combination of superior gas-barrier performance and robust antibacterial activity, rendering them promising candidates for multifunctional protective coatings and packaging applications.

Organic Solvent Resistance of the NR Composite Films

In many industrial applications, NR-based products are routinely exposed to various organic solvents, making the solvent resistance a vital performance parameter. To evaluate this property, the swelling behavior of NR, TMNR, TMNR-Eu^{3+}, GO/NR-0.5, GO/TMNR-0.5, and GO/TMNR-Eu^{3+}-0.5 composite films was examined in three representative solvents: chloroform (polar), *n*-hexane (nonpolar), and mineral oil (industrially relevant medium). The time-dependent swelling degrees are presented in Figs. 6(a)–6(c), while the corresponding maximum swelling ratios are summarized in Figs. 6(a')–6(c'). Among all the samples, GO/TMNR-Eu^{3+}-0.5 consistently exhibited the lowest swelling ratios across all solvents, indicating a superior overall solvent resistance. For instance, after 120 h of immersion in mineral oil, the swelling degree was 265.9%, which was markedly lower than that of pristine NR (525.6%) and GO/NR-0.5 (483.7%). This enhanced resistance is attributed to the combined effects of the increased crosslink density and formation of a segregated GO filler network. Such a network not only strengthens intermolecular interactions within the rubber matrix but also acts as an effective physical barrier to solvent penetration, thereby improving dimensional stability and chemical durability in organic media.

Acid and Alkali Resistance of the NR Composite Films

In addition to solvent resistance, NR-based materials in industrial and laboratory settings are frequently exposed to acidic and alkaline media, which can compromise their mechanical integri-

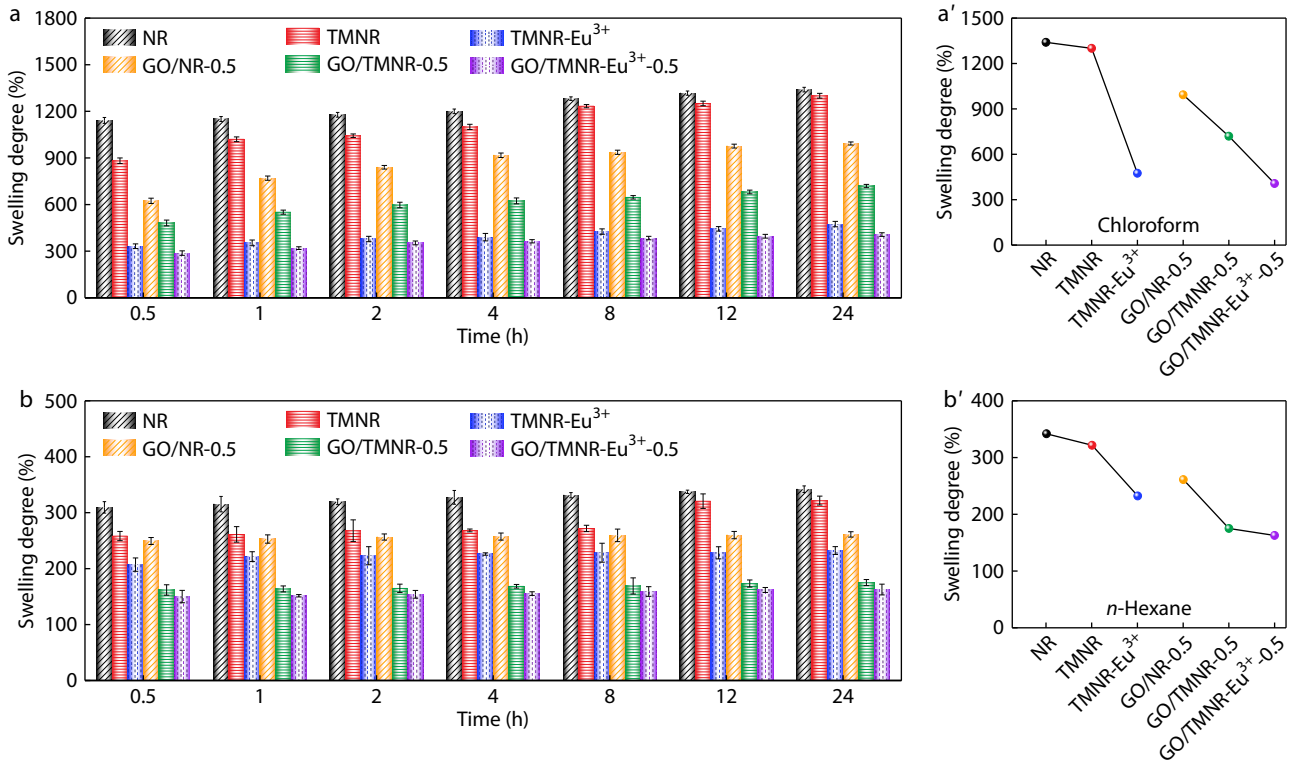

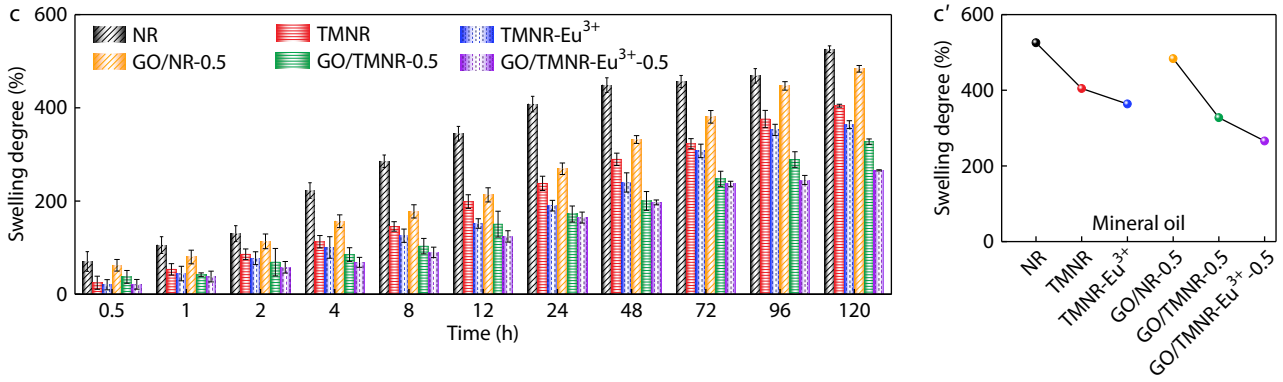

Fig. 6 Swelling degree of NR, TMNR, TMNR-Eu^{3+}, GO/NR-0.5, GO/TMNR-0.5, and GO/TMNR-Eu^{3+}-0.5 composite films in (a) chloroform, (b) *n*-hexane, and (c) mineral oil over various immersion times; The corresponding maximum swelling ratios in each solvent are summarized in (a′), (b′), and (c′).

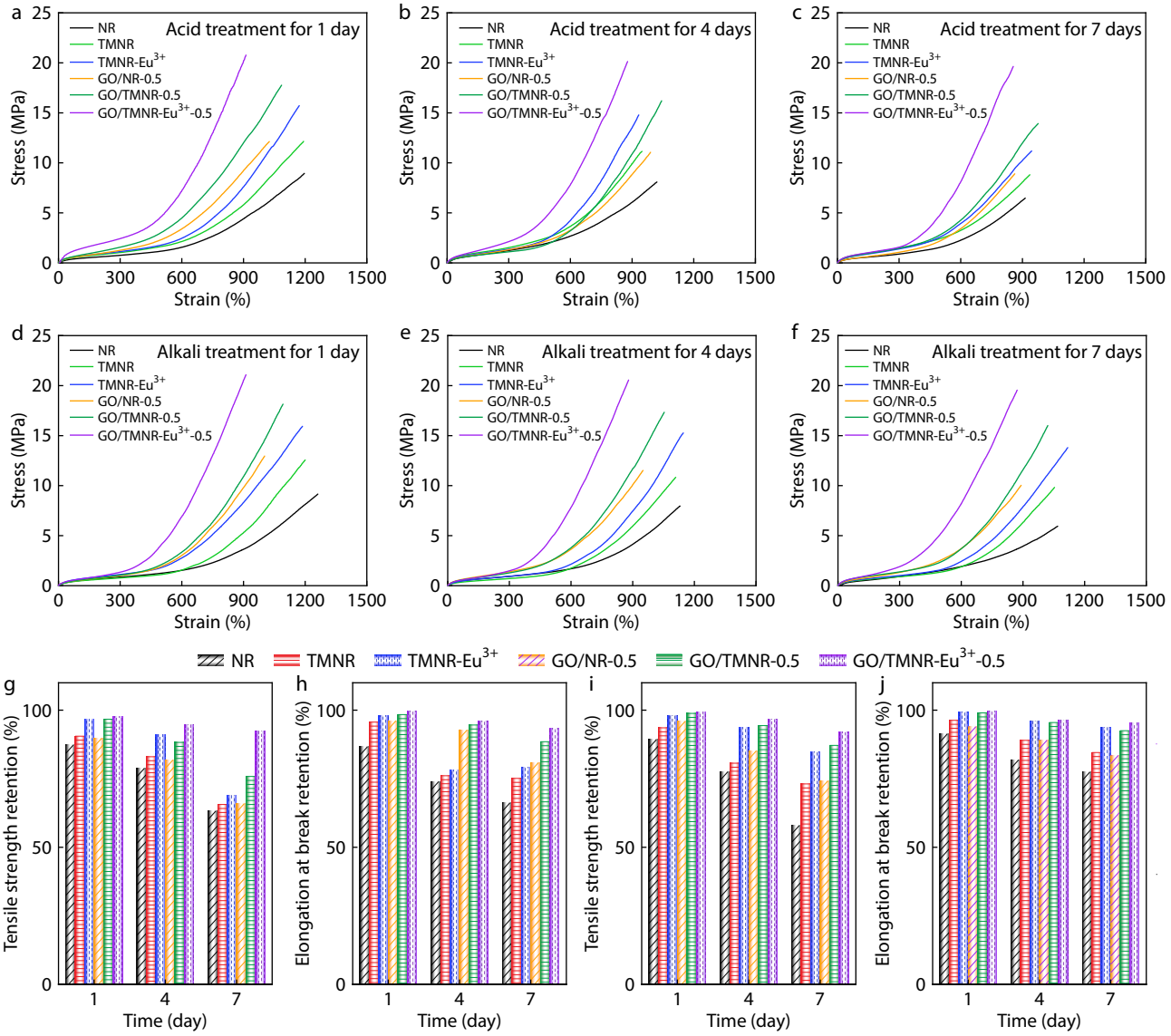

Fig. 7 Stress-strain curves of NR, TMNR, TMNR-Eu^{3+}, GO/NR-0.5, GO/TMNR-0.5, and GO/TMNR-Eu^{3+}-0.5 composite films after immersion in 0.1 mol/L HCl solution for (a) 1 day, (b) 4 days, and (c) 7 days, and after immersion in 1 mol/L NaOH solution for (d) 1 day, (e) 4 days, and (f) 7 days. Retention of (g) tensile strength and (h) elongation at break for NR, TMNR, TMNR-Eu^{3+}, GO/NR-0.5, GO/TMNR-0.5, and GO/TMNR-Eu^{3+}-0.5 composite films after immersion in 0.1 mol/L HCl solution for 1, 4, and 7 days; Retention of (i) tensile strength retention and (j) elongation at break retention of the same samples after immersion in 1 mol/L NaOH solution for 1, 4, and 7 days.

https://doi.org/10.1007/s10118-026-3580-2

ty and shorten their service life. To assess chemical stability, the composite films were immersed in acidic (0.1 mol/L HCl) and alkaline (1 mol/L NaOH) solutions for 1, 4, and 7 days, followed by tensile testing to obtain their stress-strain responses. The corresponding stress-strain curves for the acid- and alkali-treated samples are presented in Figs. 7(a)–7(c) and 7(d)–7(f), respectively. Based on these curves, the retention of tensile strength and elongation at break were calculated (Figs. 7g–7j) to evaluate their stability in acidic and alkaline environments. Pristine NR exhibited severe mechanical degradation under both conditions. After seven days in HCl, the tensile strength and elongation retention decreased to 63.2% and 66.2%, respectively. Under NaOH exposure, the corresponding values are 77.4% and 57.9%, respectively. The incorporation of GO (GO/NR-0.5) yielded moderate improvements, whereas the GO/TMNR-0.5 composite showed more substantial resistance. Notably, GO/TMNR-Eu^{3+}-0.5 achieved exceptional stability, retaining 92.5% of its tensile strength and 93.5% elongation after 7 days in HCl and 92.0% and 95.3%, respectively, after NaOH treatment. This outstanding acid-alkali resistance can be ascribed to the robust hierarchical interfacial architecture and segregated GO network, which together restrict the ingress of corrosive species into the rubber matrix, thereby minimizing molecular degradation pathways.

CONCLUSIONS

In this study, a multifunctional NR composite film was fabricated through the synergistic integration of mussel-inspired interface engineering and a segregated GO network. The incorporation of TM and Eu^{3+} ions enabled the construction of a hierarchical interfacial architecture involving covalent bonding, hydrogen bonding, and metal-ligand coordination. This strategy markedly improved GO dispersion within the rubber matrix and facilitated the formation of a structurally robust segregated network. Consequently, the optimized composite film exhibited enhanced SIC, promoting a more efficient alignment of rubber chains under deformation and contributing to superior mechanical performance. As a result, the film containing 0.5 phr GO and the bioinspired interface achieved a 107.8% increase in tensile strength, a 118.5% enhancement in tear strength, and a toughness of 61.7 MJ/m^3. In addition, the nitrogen permeability decreased by 20.1%, and the antibacterial efficiency against both *E. coli* and *S. aureus* reached 99.9%. The films also exhibited superior resistance to organic solvents and retained excellent mechanical stability in acidic and alkaline environments. These comprehensive improvements highlight the effectiveness and scalability of the proposed interfacial design strategy, which offers a promising pathway for the development of high-performance NR-based materials for medical devices, protective equipment, and industrial elastomer applications.

Conflict of Interests

The authors declare no interest conflict.

Data Availability Statement

Data supporting the findings of this study are available from the corresponding author upon reasonable request.

ACKNOWLEDGMENTS

This study was financially supported by the National Natural Science Foundation of China (No. 52303063).

REFERENCES

1 Sriring, M.; Nimpaiboon, A.; Kumarn, S.; Higaki, K.; Higaki, Y.; Kojio, K.; Takahara, A.; Ho, C. C.; Sakdapipanich, J. Film formation process of natural rubber latex particles: roles of the particle size and distribution of non-rubber species on film microstructure. *Colloid. Surfaces A* **2020**, *592*, 124571.
2 Wei, Y. C.; Xia, J.H.; Zhang, L.; Zheng, T. T.; Liao, S. Influence of non-rubber components on film formation behavior of natural rubber latex. *Colloid. Polym. Sci.* **2020**, *298*, 1263–1271.
3 Ng, J. W.; Othman, N.; Yusof, N. H. Various coagulation techniques and their impacts towards the properties of natural rubber latex from Hevea brasiliensis—a comprehensive review related to tyre application. *Ind. Crop. Prod.* **2022**, *181*, 114835.
4 Zhang, G.; Guo, B.; Zhang, L. Significant trends in rubber research driven by environment, resource, and sustainability. *Macromolecules* **2025**, *58*, 5883–5903.
5 Whba, R.; Su'ait, M. S.; Whba, F.; Sahinbay, S.; Altin, S.; Ahmad, A. Intrinsic challenges and strategic approaches for enhancing the potential of natural rubber and its derivatives: a review. *Int. J. Biol. Macromol.* **2024**, *276*, 133796.
6 Sethulekshmi, A. S.; Saritha, A.; Joseph, K. A comprehensive review on the recent advancements in natural rubber nanocomposites. *Int. J. Biol. Macromol.* **2022**, *194*, 819–842.
7 Hou, J.R.; Huang, S. S.; Zhang, N.; Liu, D. Y.; Zhang, Z. J.; Yang, H. S.; Zong, L.; Duan, Y. X.; Zhang, J. M. Reinforcing natural rubber by amphiphilic graphene oxide for high-performance catheters. *Polymer* **2021**, *232*, 124142.
8 Yang, W.; Liu, J. J.; Wang, L. L.; Wang, W.; Yuen, A. C. Y.; Peng, S.; Yu, B.; Lu, H. D.; Yeoh, G. H.; Wang, C. H. Multifunctional MXene/natural rubber composite films with exceptional flexibility and durability. *Compos. Part B-Eng.* **2020**, *188*, 107875.
9 Hosseinmardi, A.; Amiralian, N.; Hayati, A. N.; Martin, D. J.; Annamalai, P. K. Toughening of natural rubber nanocomposites by the incorporation of nanoscale lignin combined with an industrially relevant leaching process. *Ind. Crop. Prod.* **2021**, *159*, 113063.
10 Li, J.; Liu, G.; Liu, Y.; Wu, Y.; He, M.; Li, Y. Cellulose fiber-assisted construction of multifunctional natural rubber latex sponges with excellent water-responsive shape memory behavior and oil absorption properties using ice template-vulcanization technology. *Int. J. Biol. Macromol.* **2025**, *308*, 142505.
11 Luo, C.; Xu, Y.; Jin, H. Preparation of biomass-oxidized natural rubber/cellulose nanofibers composites with enhanced mechanical properties and self-healing properties based on hydrogen bonding network. *Ind. Crop. Prod.* **2025**, *226*, 120628.
12 Gong, H.; Zhong, K.; Chen, F.; Yi, M.; Wan, L.; Wang, Z.; Liao, J. Preparation of modified hydroxyapatite and its effect on natural latex film. *J. Appl. Polym. Sci.* **2023**, *140*, e54019.
13 Liu, C.; Huang, S.; Hou, J.; Zhang, W.; Wang, J.; Yang, H.; Zhang, J. Natural rubber latex reinforced by graphene oxide/zwitterionic chitin nanocrystal hybrids for high-performance elastomers without sulfur vulcanization. *ACS Sustain. Chem. Eng.* **2021**, *9*, 6470–6478.
14 Szadkowski, B.; Rybiński, P.; Sarlin, E.; Marzec, A. Bio-functionalization of fillers with natural phytic acid for sustainable flame-retardant agents for natural rubber composites. *Ind. Crop.*

Graphical Abstract

Synergistic Bioinspired Interface and Segregated Graphene Oxide Networks Enabling Enhanced Mechanical Strength and Chemical Resistance in Natural Rubber Latex Composites

Xiao-Da Pan, Yun-Kui Song, Chong-Zhi Sun, Chao-Yang Yuan, Zong-Min Zhu, Jia-Ran Wang, Xian-Ze Yin, Hong-Tao Liu, Li Liu, and Long Zheng

Wuhan Textile University; Beijing University of Chemical Technology

A mussel-inspired interfacial regulation strategy was developed by designing a catechol- and thiol-containing tannic acid-based modifier (TM) agent that induces graphene oxide (GO) to self-assemble on natural rubber (NR) latex particles into a segregated network, while Eu^{3+} coordination synergistically reinforces the interface. This structure markedly promotes NR strain-induced crystallization and enhances mechanical, barrier, antibacterial, and chemical-resistant properties.

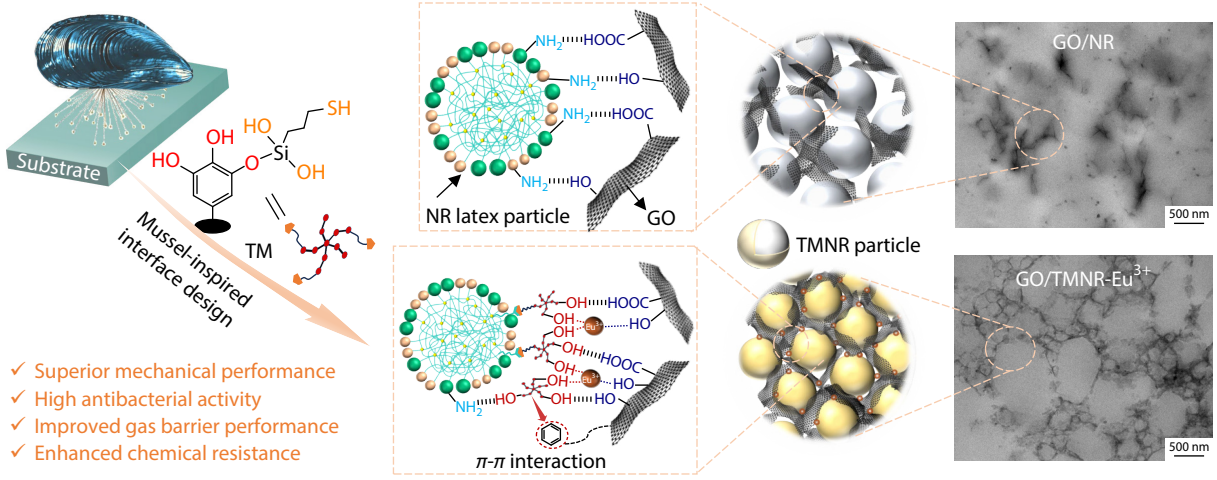

Chinese J. Polym. Sci. 2026, 44, 1186–1198 *https://doi.org/10.1007/s10118-026-3580-2*

Prod. **2024**, *222*, 119504.
15 Kargarzadeh, H.; Mariano, M.; Huang, J.; Lin, N.; Ahmad, I.; Dufresne, A.; Thomas, S. Recent developments on nanocellulose reinforced polymer nanocomposites: a review. *Polymer* **2017**, *132*, 368–393.
16 Wang, L.; Zhang, J.; Yang, G.; Sun, Y.; Liang, Y.; Wang, Y.; Li, C. Self-crosslinking of graphene oxide/natural rubber nanocomposite film under assistance of protein for enhancing gas barrier performance. *Surf. Interfaces* **2021**, *26*, 101359.
17 Xing, W.; Wu, J.; Huang, G.; Li, H.; Tang, M.; Fu, X. Enhanced mechanical properties of graphene/natural rubber nanocomposites at low content. *Polym. Int.* **2014**, *63*, 1674–1681.
18 George, N.; C. S, J. C.; Mathiazhagan, A.; Joseph, R. High performance natural rubber composites with conductive segregated network of multiwalled carbon nanotubes. *Compos. Sci. Technol.* **2015**, *116*, 33–40.
19 George, N.; Varghese, G. A.; Joseph, R. Improved mechanical and barrier properties of Natural rubber-Multiwalled carbon nanotube composites with segregated network structure. *Mater. Today: Proc.* **2019**, *9*, 13–20.
20 George, N.; Bipinbal, P.; Bhadran, B.; Mathiazhagan, A.; Joseph, R. Segregated network formation of multiwalled carbon nanotubes in natural rubber through surfactant assisted latex compounding: A novel technique for multifunctional properties. *Polymer* **2017**, *112*, 264–277.
21 Zhu, Y.; Wei, L.Y.; Fu, X.; Zhang, J. Q.; Kong, L. M.; Huang, G. S.; Wu, J. R. Super strong and tough elastomers enabled by sacrificial segregated network. *Chinese J.Polym. Sci.* **2020**, *39*, 377–386.
22 Zheng, S.; Wang, Y.; Zhu, Y.; Zheng, C. Recent advances in the construction and properties of carbon-based nanofillers/polymer composites with segregated network structures. *Mater. Today Commun.* **2023**, *36*, 106773.
23 Pan, G.; Li, B. A dynamic biointerface controls mussel adhesion. *Science* **2023**, *382*, 763–764.
24 Zhang, C.; Xiang, L.; Zhang, J.; Liu, C.; Wang, Z.; Zeng, H.; Xu, Z.-K. Revisiting the adhesion mechanism of mussel-inspired chemistry. *Chem. Sci.* **2022**, *13*, 1698–1705.
25 Huang, S.; Zhang, J.; Kong, L.; Li, W.; Xie, Z. T.; Wu, J. Fully biosourced, vulcanization-free, and thermal-responsive natural rubber material. *Macromolecules* **2024**, *57*, 1642–1652.
26 Wei, Y. C.; Liu, G. X.; Zhang, L.; Xu, W. Z.; Liao, S.; Luo, M. C. Mimicking the mechanical robustness of natural rubber based on a sacrificial network constructed by phospholipids. *ACS Appl. Mater. Interfaces* **2020**, *12*, 14468–14475.
27 Zhu, S.; Zhao, F.; Sun, Y.; Wang, C.; Yuan, Z.; Liao, S. Fluorinated natural rubber with enhanced strength and excellent resistance to ozone, organic solvent, and acid and alkali via in situ reactive melt extrusion. *Polym. Degrad. Stabil.* **2024**, *228*, 110916.

28 Zhou, Z.; Liu, T.; Zhou, W.; Chen, H.; Bian, Y.; Gong, S.; Shi, S. Q.; Li, J. A strong and biodegradable wood particles-based bioplastic modified by synergistically dynamic cross-linking with tannic acid and Fe3+. *Compos. Part B-Eng.* **2022**, *247*, 110349.
29 Li, Z.; Liu, R.; Zhang, Y.; Yang, K.; Zhang, Z.; Zhao, Y.; Yan, H. Designing schiff-based hyperbranched polysiloxane for simultaneously enhancing epoxy resin with mechanical properties, thermal stability, and recyclability. *ACS Appl. Polym. Mater.* **2024**, *6*, 3115–3127.
30 Li, H.; Gao, C.; Tang, L.; Wang, C.; Chen, Q.; Zheng, Q.; Yang, S.; Sheng, S.; Zan, X. Lysozyme (Lys), tannic acid (TA), and graphene oxide (GO) thin coating for antibacterial and enhanced osteogenesis. *ACS Appl. Bio Mater.* **2020**, *3*, 673–684.
31 Boro, U.; Karak, N. Tannic acid based hyperbranched epoxy/reduced graphene oxide nanocomposites as surface coating materials. *Prog. Org. Coat.* **2017**, *104*, 180–187.
32 Quevedo, B. V.; Komatsu, D.; de Lourdes Rezende, M.; de Rezende Duek, E. A. Synthesis of epoxidized natural rubber grafted with hyaluronic acid for the development of biomaterials. *Int. J. Biol. Macromol.* **2023**, *244*, 125359.
33 Qiu, H.; Ni, W.; Yang, L.; Zhang, Q. Remarkable ability of Pb(II) capture from water by self-assembled metal-phenolic networks prepared with tannic acid and ferric ions. *Chem. Eng. J.* **2022**, *450*, 138161.
34 Li, S.; Liang, F.; Zhou, J.; Shi, B. Bio-inspired dual crosslinked network mediated by plant polyphenols for toughening natural rubber latex-based elastomeric composites. *Ind. Crop. Prod.* **2024**, *210*, 118027.
35 Dong, G.; Liu, H.; Yu, X.; Zhang, X.; Lu, H.; Zhou, T.; Cao, J. Antimicrobial and anti-biofilm activity of tannic acid against Staphylococcus aureus. *Nat. Prod. Res.* **2018**, *32*, 2225–2228.
36 Sethulekshmi, A. S.; Joseph, K.; Aprem, A. S.; Sisupal, S. B.; Punetha, V. D.; Saritha, A. Green synthesis of tannic acid-modified tungsten disulfide nanosheets: a cost effective pathway towards tailoring the properties of natural rubber. *Tungsten* **2025**, 1–14.

https://doi.org/10.1007/s10118-026-3580-2